Chapter 4
Tides in Coastal Seas. Influence of Topography and Bottom Friction

Pieter C. Roos and Huib E. de Swart

Abstract Tides are important in various ways, e.g., by affecting navigation and coastal safety and by acting as a driver for sediment transport and seabed dynamics. To explain spatial patterns of tidal phase and range, observed in coastal seas around the world, we present an idealised process-based model. It solves the depth-averaged linearised shallow water equations, including the Coriolis effect and bottom friction, on schematised geometries with rectilinear coastlines and stepwise topographic variations. Based on an extended Klein-Gordon equation (accounting for bottom friction), Kelvin and Poincaré modes are identified as the fundamental wave solutions in a channel of uniform width and depth. We analyse their spatial structures and dynamic properties, addressing the roles of bottom friction and transverse topographic steps. The solution for a semi-enclosed basin, including topographic steps, is then obtained as a superposition of these wave modes, by applying a collocation technique. As an example, we present solutions that grossly explain the amphidromic system of the Gulf of California. Finally, we discuss the modelling approach and address the links with morphodynamics and climate change.

4.1 Introduction

Tides are the periodic water oscillations driven by the gravitational attraction of the moon and the sun. They constitute a fascinating phenomenon of both academic and practical interest.

To clarify this, it is useful to distinguish between 'vertical' and 'horizontal' tides. The *vertical tide* concerns the rise and fall of the free surface, with the difference between high and low water known as tidal range H. Figure 4.1 shows an example
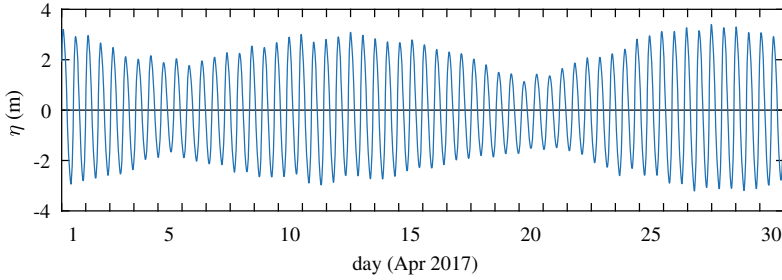
P. C. Roos (✉)
Water Engineering & Management, University of Twente, Enschede, The Netherlands
e-mail: p.c.roos@utwente.nl

H. E. de Swart
Institute for Marine and Atmospheric research, Department of Physics, Utrecht University, Utrecht, The Netherlands
e-mail: h.e.deswart@uu.nl

Fig. 4.1 Tidal record at Dover, UK, showing observed surface elevation versus time for April 2017. Mean elevation over this period used as vertical datum. Data from British Oceanographic Data Centre

of a tidal record at Dover, UK, with $H \sim 3 - 6$ m. It is dominated by a semi-diurnal cycle and further subject to other variations (spring-neap cycle, daily inequality) and weather effects. These water levels are important for coastal safety and for navigation, with so-called tidal windows allowing ship access to channels and harbours.

The *horizontal tide* refers to the oscillatory currents that are dynamically coupled to the vertical tide. In the North Sea, such currents are in the order of $0.1 - 1$ m s^{-1} (Davies and Kwong 2000). Apart from directly affecting navigation, tidal currents also have indirect implications. By eroding and transporting sand, they shape the seabed, thereby creating bed forms such as tidal sandbanks (De Swart and Yuan 2019) and sand waves (Besio et al. 2008). Also, by transporting other matter (mud, salt and nutrients), tidal currents affect turbidity, salt intrusion and the residence time of nutrients, which is important for water quality and ecology.

Let us now turn to tidal observations in more detail, particularly their temporal and spatial structure. Harmonic analysis enables decomposition of the tidal signal into different constituents. For the free surface elevation η as a function of time t, we may thus write

$$\eta = \sum_{n=1}^{N} \tfrac{1}{2} H_{c_n} \cos(\sigma_{c_n} t - \varphi_{c_n}), \tag{4.1}$$

thereby distinguishing N constituents c_n, each with an individual tidal range H_{c_n}, angular frequency σ_{c_n} and phase φ_{c_n}. Similar expressions hold for the components of the tidal current. The constituents include those directly following from celestial mechanics and those indirectly resulting from their nonlinear interaction (Parker 1993). Instead of a detailed derivation involving the tidal potential (Platzman 1982; Gerkema 2019), here we simply consider them as given (e.g., M2, S2, K1, O1; see Table 4.1) and mostly focus on the dominant one.

Observations from coastal seas around the world reveal intriguing spatial variations in tidal range and phase, so

$$H_{c_n} = H_{c_n}(x, y), \qquad \varphi_{c_n} = \varphi_{c_n}(x, y), \tag{4.2}$$

Table 4.1 Overview of the tidal constituents addressed in this chapter

Name c_n	Description	Period T (h)	Angular frequency	
			σ (rad s^{-1})	σ/σ_{M2} (-)[a]
M2	Principal lunar semi-diurnal component	12.42	1.405×10^{-4}	1
S2	Principal solar semi-diurnal component	12.00	1.454×10^{-4}	1.035
K1	Luni-solar diurnal component	23.93	7.293×10^{-5}	0.519
O1	Principal lunar diurnal component	25.82	6.759×10^{-5}	0.481

[a]Relative to the angular frequency of the M2-tide

where we have introduced horizontal coordinates x and y. These patterns are visualised in so–called *amphidromic charts*, showing co-range and co-phase lines for a given constituent (Figs. 4.2 and 4.3). From the examples shown, we highlight the following features.

- Behaviour as a progressive wave along the coast, with a wavelength in the order of hundreds of kilometres. At the UK East Coast, for example, co-range lines are roughly parallel and co-phase lines perpendicular to the coastline.
- Cross-shore decay of tidal range with a typical length scale of about hundred kilometres in the North Sea.
- Cyclonic rotation[1] around locations with vanishing tidal range, known as (elevation) *amphidromic points*. These points can be real (inside basin) or virtual (outside basin, as in the Gulf of California).[2]
- In some cases, significant amplification of tidal range towards the shallow region at the head of the basin, such as in the Gulf of California.
- Local flow structure showing ellipses near closed end and bidirectional flow further away.

The goal of this chapter is to provide a generic process-based explanation of the amphidromic patterns observed in coastal seas as presented above. To position our work, we focus on barotropic tides[3] in basins that, from a dynamical point of view, can be termed both *shallow* and *wide*. These properties, to be quantified in the subsequent analysis, have implications for wave speed ('shallow') and emphasize

---

[1] Cyclonic means counterclockwise in the Northern Hemisphere and clockwise in the Southern Hemisphere.

[2] Next to these elevation amphidromic points, there are also *current amphidromic points*, i.e. locations where the tidal current ellipse reduces to a circle (Zongwan et al. 1995).

[3] Barotropic tides are associated with motion that is driven by gradients in sea level only; they are not affected by pressure gradient forces that result from density stratification. In the absence of friction, barotropic motion has no vertical structure.
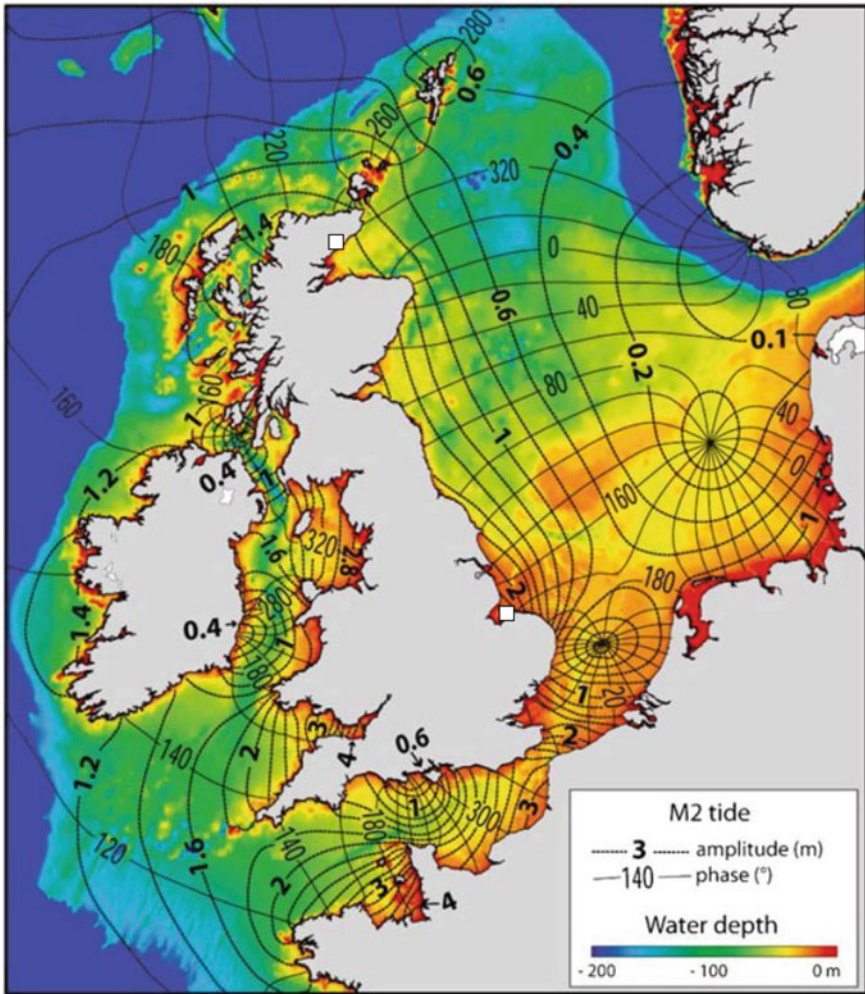
Fig. 4.2 Amphidromic chart of the semi-diurnal lunar tide (M2) in the North Sea, showing co-amplitude lines (half the tidal range) in m and co-phase lines in degrees. Colours in the background indicate water depth (Reynaud and Dalrymple 2012, after Sinha and Pingree 1997). Reprinted by permission from Springer: Springer, Principles of Tidal Sedimentology by R.A. Davis Jr. and R.W. Dalrymple, copyright (2012). The white squares along the UK East Coast denote the two tide stations Helmsdale (top) and Hunstanton (bottom) referred to in Sect. 4.3.2

the roles of bottom friction ('shallow') and the Coriolis effect ('wide'). As a result, we exclude narrow estuaries and tidal channels (or networks), for which lateral uniformity permits a cross-sectionally averaged approach (Friedrichs 2010; Talke and Jay 2020). Furthermore, as the basins are much smaller than the wavelength of
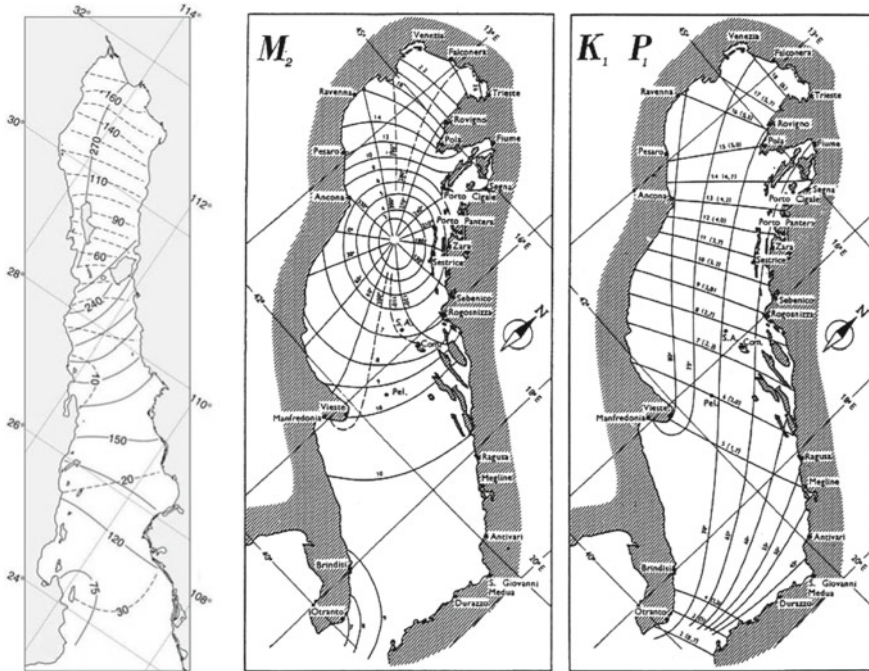
Fig. 4.3 Examples of amphidromic patterns from coastal seas around the world. Left: M2-tide in the Gulf of California, Mexico (Salas-de León et al. 2003), with co-phase in degrees (solid) and co-range in cm (dashed). Reprinted with permission from the American Geophysical Union. Middle and right: M2 and K1/P1 tides in the Adriatic Sea, with phase in degrees and range in cm, according to Polli (1960)

the directly forced tide (typically half the earth's circumference), they effectively *co-oscillate* with the tides in the adjacent larger oceans.

To achieve our goal, we adopt a so-called idealised process-based modelling approach, in which model geometry and the physical laws of water motion are both schematised, enabling analytical solutions that provide maximum insight. Specifically, we shall consider the linearised depth-averaged shallow water equations on the f plane, including bottom friction, in water bodies with rectilinear coastlines and step-wise topographic variations. Co-oscillation implies that the tidal potential can be neglected, so the system is forced only by elevations and/or currents at the open boundaries. Mathematically speaking, nonhomogeneities appear in the (open) boundary conditions rather than in the differential equations. In comparison to other texts on this topic (Pedlosky 1987; Gerkema 2019), the combined inclusion of bottom friction and topographic variations is the main innovation.

This chapter is organised as follows. Section 4.2 presents the model formulation, including the underlying assumptions and geometry. Then, in Sect. 4.3, we derive Kelvin and Poincaré modes as fundamental wave solutions in a channel section of uniform width and depth. Section 4.4 then demonstrates how superposition of these
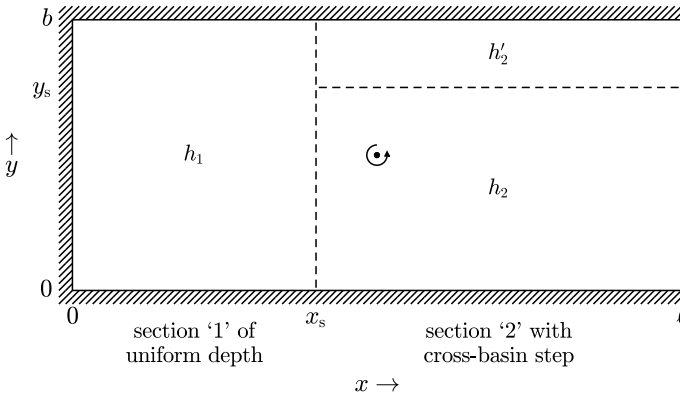
Fig. 4.4 Definition sketch of model geometry (top view), showing a semi-enclosed basin of length ℓ and width b. Along-basin and cross-basin topographic steps are denoted with dashed lines at $x = x_s$ and $y = y_s$, compartment depths with h_j and h'_j. In this example, we thus identify a section of uniform depth ($j = 1$) and a section with a single cross-basin step ($j = 2$). The open boundary at $x = \ell$ is represented by a dotted line

modes explains the amphidromic patterns occurring in large-scale basins with a specific topography. Section 4.5 contains a discussion of physical processes, implications (morphodynamics, climate change) and the model approach. Finally, we present our conclusions in Sect. 4.6.

4.2 Model Formulation

In our idealised process-based model, we consider a semi-enclosed rectangular basin of uniform width b and length ℓ (Fig. 4.4). Introducing along-basin and cross-basin coordinates x and y, the closed boundaries are located at $y = 0, b$ and $x = 0$. The depth h is spatially uniform, except across topographic steps, which are allowed parallel to either the x- or y-direction.

Let us now turn to the description of the flow. We assume that the density ρ is constant, which makes the free surface elevation η, defined with zero spatial average, the primary variable of interest. As the horizontal scales of interest (tens to hundreds of km) are much larger than the vertical ones (tens to hundreds of m), we assume *shallow water flow* by which pressure gradients are proportional to gradients of the free surface elevation. Furthermore, we will not consider the vertical structure of the tide. We let u and v denote the *depth-averaged* velocity components in x- and y-direction, respectively.

Next, we make the following assumptions about the relevant processes. First, to account for the *Coriolis effect*, the f plane approximation is adopted, with a Coriolis parameter that is set to a constant value

$$f = 2\Omega \sin \theta. \tag{4.3}$$

Here, $\Omega = 7.292 \times 10^{-5}$ rad s^{-1} is the angular frequency of the earth's rotation and θ is latitude. Second, we consider *linearised dynamics* because the Froude number Fr $= U/(gh)^{1/2}$ is small (with velocity scale U and gravitational acceleration $g = 9.81$ m s^{-2}). This implies that the nonlinear advective terms can be neglected, as well as the contribution of the free surface displacement to the total water depth, i.e. $h + \eta \approx h$. Furthermore, we include *bottom friction* with the bed shear stress parameterised in a linear way (Prandle 1982). Finally, *co-oscillation* implies that the direct tidal forcing from the tidal potential is neglected.

With the above assumptions, the momentum and continuity equations are given by

$$\underbrace{\frac{\partial u}{\partial t} + \frac{ru}{h}}_{\mathcal{L}u} - fv = -g\frac{\partial \eta}{\partial x}, \tag{4.4a}$$

$$\underbrace{\frac{\partial v}{\partial t} + \frac{rv}{h}}_{\mathcal{L}v} + fu = -g\frac{\partial \eta}{\partial y}, \tag{4.4b}$$

$$\frac{\partial \eta}{\partial t} + h \left(\frac{\partial u}{\partial x} + \frac{\partial v}{\partial y} \right) = 0. \tag{4.4c}$$

Here, r is a linear friction coefficient (Prandle 1982), f the Coriolis parameter specified in Eq. (4.3) and g the gravitational acceleration. To facilitate the subsequent analysis, we have introduced the differential operator $\mathcal{L} = \frac{\partial}{\partial t} + \frac{r}{h}$, which combines inertial and frictional terms in the momentum equations.

At closed boundaries, the normal velocities must vanish. For the geometries under consideration, this boils down to

$$v = 0 \quad \text{at } y = 0, b, \tag{4.5a}$$
$$u = 0 \quad \text{at } x = 0. \tag{4.5b}$$

Our model is forced at its open boundary. For a given constituent with angular frequency σ, we prescribe the cross-basin profiles of tidal range H and phase φ:

$$\eta = \tfrac{1}{2} H(y) \cos \left(\sigma t - \varphi(y) \right) \quad \text{at } x = \ell. \tag{4.6}$$

Across topographic steps, we require continuity of elevation and normal transport. Depending on the type of step (longitudinal at $x = x_s$ or lateral at $y = y_s$), this is written as

$$\lim_{x \uparrow x_s}(\eta, hu) = \lim_{x \downarrow x_s}(\eta, hu), \tag{4.7a}$$

$$\lim_{y \uparrow y_s}(\eta, hv) = \lim_{y \downarrow y_s}(\eta, hv). \tag{4.7b}$$

Keeping the regular nature of tides in mind, we seek time-periodic solutions in dynamic equilibrium with the boundary forcing in Eq. (4.6). This means that the transient motion generated by starting from a certain initial condition has damped out due to bottom friction.

4.3 Fundamental Wave Solutions

In this section, we seek wave solutions in a channel section of uniform width. Our derivation, which involves the Klein-Gordon equation (Sect. 4.3.1), leads to the identification of the Kelvin wave (Sect. 4.3.2) and Poincaré waves (Sect. 4.3.3). The analysis is presented for a channel with uniform depth; the case with a single transverse step is treated separately in Sect. 4.3.4 (Roos and Schuttelaars 2009). We closely follow Pedlosky (1987), but extend it to account for bottom friction and a transverse topographic step.

4.3.1 Derivation with Klein-Gordon Equation

Let $\phi = (\eta, u, v)$ symbolically denote the state of the system. For a given frequency σ, we write

$$\phi = \text{Re}\left\{\tilde{\phi}(y) \exp(i[kx - \sigma t])\right\}, \tag{4.8}$$

with complex amplitudes $\tilde{\phi}(y) = (\tilde{\eta}(y), \tilde{u}(y), \tilde{v}(y))$ that are functions of the cross-channel coordinate y, and $\text{Re}\{\cdot\}$ denoting the real part. The wave number $k = k_r + ik_i$, also complex, is to be determined from the analysis below. The boundary conditions are as in Eq. (4.5a); they imply $\tilde{v}(0) = \tilde{v}(b) = 0$.

Before proceeding, we first derive an important general result.

We start by deriving the so-called *polarisation equations*, which relate the individual velocity components to the free surface elevation:

$$\left(\mathcal{L}^2 + f^2\right) u = -g\mathcal{L}\frac{\partial \eta}{\partial x} - fg\frac{\partial \eta}{\partial y}, \tag{4.9a}$$

$$\left(\mathcal{L}^2 + f^2\right) v = -g\mathcal{L}\frac{\partial \eta}{\partial y} + fg\frac{\partial \eta}{\partial x}. \tag{4.9b}$$

They follow from eliminating either v or u from the momentum equations (4.4a)–(4.4b).

Then, multiplying Eqs. (4.9) with h, taking their divergence and applying the continuity equation (4.4c) leads to a single equation for η only. This is the 'extended' *Klein-Gordon equation*:

$$\left(\mathcal{L}^2 + f^2\right)\frac{\partial \eta}{\partial t} - gh\mathcal{L}\left(\frac{\partial^2 \eta}{\partial x^2} + \frac{\partial^2 \eta}{\partial y^2}\right) = 0, \tag{4.10}$$

here, unlike its classical formulation, accounting for bottom friction. It serves as the governing equation for the wave solutions derived in this section. To arrive at Eq. (4.10), it is essential that h and r are spatially uniform. In the case without bottom friction ($r = 0$, so $\mathcal{L} = \frac{\partial}{\partial t}$), time integration of Eq. (4.10), while assuming wave-like solutions, recovers the regular Klein-Gordon equation (Pedlosky 1987). If also the Coriolis effect were neglected ($f = 0$), this would further reduce to the classical shallow-water wave equation $\frac{\partial^2 \eta}{\partial t^2} - gh\left(\frac{\partial^2 \eta}{\partial x^2} + \frac{\partial^2 \eta}{\partial y^2}\right) = 0$. As can be shown, also the flow velocity components must satisfy the extended Klein-Gordon equation, so in Eq. (4.10) one may freely replace η with either u or v.

The next step is to substitute our solution (4.8) into the extended Klein-Gordon equation (4.10). Upon defining the complex frictional correction factor

$$\gamma = \sqrt{1 + i\mu}, \qquad \text{with } \mu = \frac{r}{\sigma h}, \tag{4.11}$$

implying $\gamma = 1$ in the absence of friction, it follows that $\mathcal{L} = -i\gamma^2\sigma$ and we find

$$\frac{\partial^2 \tilde{\eta}}{\partial t^2} + \alpha^2 \tilde{\eta} = 0, \qquad \text{with } \alpha^2 = \frac{\gamma^2 \sigma^2 - \gamma^{-2} f^2}{gh} - k^2. \tag{4.12}$$

The general solution to this differential equation reads

$$\tilde{\eta}(y) = A\cos\alpha y + B\sin\alpha y, \tag{4.13}$$

with constants A and B that follow from the boundary conditions in Eq. (4.5a). With the aid of the polarisation equation (4.9b), these are written in matrix form according to

$$\begin{bmatrix} fk & \alpha\gamma^2\sigma \\ fk\cos\alpha b - \alpha\gamma^2\sigma\sin\alpha b & \alpha\gamma^2\sigma\cos\alpha b + fk\sin\alpha b \end{bmatrix} \begin{bmatrix} A \\ B \end{bmatrix} = \begin{bmatrix} 0 \\ 0 \end{bmatrix}. \quad (4.14)$$

This system has non-trivial solutions only if the determinant of the coefficient matrix vanishes. With the definition of the parameter α in Eq. (4.12), we obtain the following condition:

$$\left([\gamma^2\sigma]^2 - f^2 \right) \left(k^2 - \frac{\gamma^2\sigma^2}{gh} \right) \sin\alpha b = 0. \quad (4.15)$$

This equation contains three roots. The second and third are associated with Kelvin and Poincaré waves, to be analysed in the following subsections. In doing so we will adopt parameter values, inspired by the coastal seas of Sect. 4.1 and further aimed at exposing the key properties (Table 4.2). The first only exists without bottom friction; in that case it has been shown to add no information to the Kelvin wave (Pedlosky 1987).

4.3.2 Kelvin Wave

The second root in Eq. (4.15) corresponds to the so-called *Kelvin wave*. It permits two values of the wave number, i.e.

$$k = k_0^\oplus = +\gamma K, \qquad k = k_0^\ominus = -\gamma K, \qquad \text{with } K = \frac{\sigma}{\sqrt{gh}}, \quad (4.16)$$

corresponding to a progressive wave travelling in either the positive or negative x-direction. The wave number equals that of a shallow water wave ($\pm K$), modified by the frictional correction factor γ defined in Eq. (4.11). A subscript '0' has been added, because, as we shall see in Sect. 4.3.3, the Kelvin wave serves as the lowest mode in a family of wave solutions.

Using Eq. (4.16), the coefficient in Eq. (4.12) reduces to $\alpha = \pm i\gamma^{-1}f(gh)^{-1/2}$. The elevation and velocity amplitudes, as defined in Eq. (4.8), are given by

$$\tilde{\phi}_0^\oplus = \left(\tilde{\eta}_0^\oplus, \tilde{u}_0^\oplus, \tilde{v}_0^\oplus \right) = (Z, U, 0)\exp\left(\frac{-fy}{\gamma\sqrt{gh}} \right), \quad \text{with } U = \frac{Z}{\gamma}\sqrt{\frac{g}{h}}, \text{(4.17a)}$$

$$\tilde{\phi}_0^\ominus = \left(\tilde{\eta}_0^\ominus, \tilde{u}_0^\ominus, \tilde{v}_0^\ominus \right) = (Z, -U, 0)\exp\left(\frac{-f[b-y]}{\gamma\sqrt{gh}} \right). \quad (4.17b)$$

Table 4.2 Overview of model parameters and values (as used in Figs. 4.5, 4.7, 4.8, 4.9 and 4.10)

Symbol	Description	Value	Unit(s)
h	Water depth*	20	m
θ	Latitude	50	°N
σ	Angular frequency	1.405×10^{-4}	rad s^{-1}
r	Friction coefficient	5.0×10^{-4}	m s^{-1}
b	Channel/basin width	300[Fig. 4.5], 700[Figs. 4.7,4.8], 200[Figs. 4.9,4.10]	km
ℓ	Basin length[Fig. 4.10]	600	km
x_s	Position of along-basin step[Fig. 4.10]	150	km
f	Coriolis parameter, Eq. (4.3)	1.12×10^{-4}	rad s^{-1}
μ	Dimensionless friction coefficient, Eq. (4.11)	0.18	–
K	Shallow water wave number, Eq. (4.16)	1.00×10^{-5}	rad m^{-1}
R	Rossby deformation radius, Eq. (4.18)	125	km
b_{crit}	Critical channel width, Eq. (4.23)	519	km
λ_0	Kelvin wavelength	626[†Figs. 4.5a,4.9a], 624[Figs. 4.5b,4.9b]	km
λ_1	Wavelength of 1st Poincaré mode[†‡Fig. 4.7a]	1584	km
L_2	Decay length of 2nd Poincaré mode[†‡Fig. 4.7b]	149	km
L_3	Decay length of 3rd Poincaré mode[†‡]	83	km

*N.B.: in Fig. 4.10 we use a reference depth of $h = 40$ m and a shallow region of $h = 20$ m),
[†]Without bottom friction, [‡]For channel width $b = 700$ km.

In these expressions, Z represents the coastal elevation amplitude[4] at $(x, y) = (0, 0)$ and $(0, b)$, respectively, and U is the coastal velocity amplitude.

Let us now highlight the key properties of the Kelvin wave (Fig. 4.5, using parameter values from Table 4.2), first for the case without bottom friction ($r = 0$, so $\gamma = 1$, Fig. 4.5a):

- Nondispersive progressive shallow water wave with wave speed $(gh)^{1/2}$ and the along-channel velocity in phase with the free surface elevation.
- Exponential decay in the cross-channel direction with the so-called *Rossby deformation radius*

---

[4] For $f > 0$, Z is the *maximum* elevation amplitude of the Kelvin wave as it decreases when moving to the other coast. Conversely, for $f < 0$, Z is the *minimum* coastal amplitude.

a Kelvin wave (without friction) **b** Kelvin wave (with friction)
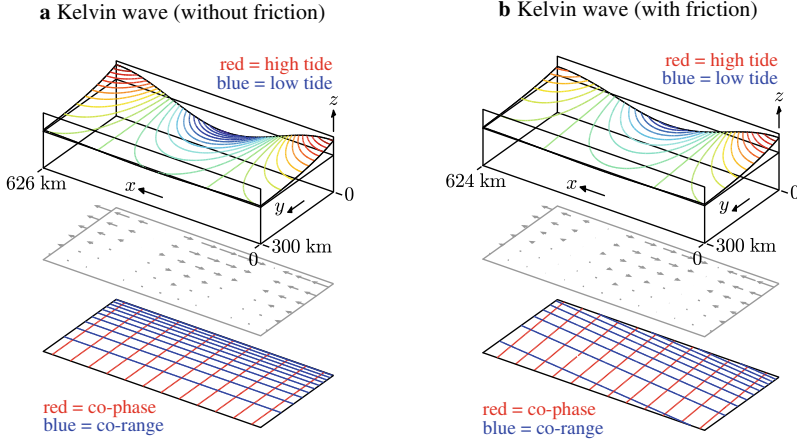
Fig. 4.5 Visualisation of Kelvin wave in a channel section of uniform width and depth in the Northern Hemisphere, propagating from right to left: **a** without friction, **b** with friction. The top panels show a three-dimensional snapshot of the surface elevation (coloured contours, high tide in red and low tide in blue). The middle panels show the corresponding instantaneous depth-averaged velocity (grey arrows). The bottom panels show the co-range lines (blue) and co-phase lines (red). Parameter values as in Table 4.2, with the frictional case chosen such that amplitude decay in the direction of propagation is already visible over one wavelength

$$R = \frac{\sqrt{gh}}{|f|} \tag{4.18}$$

as e-folding length scale. This enables us to quantify the 'wide' basins mentioned in the Introduction as basins with $b = \mathcal{O}(R)$ (or larger). For $b \ll R$, the cross-channel structures in Eq. (4.17) are nearly uniform, indicating that the Coriolis effect only marginally affects the solution.

- Facing the direction of propagation, the Kelvin wave 'hugs' the coast on its right (Northern Hemisphere, Fig. 4.5a) or on its left (Southern Hemisphere).
- Vanishing cross-channel velocity, i.e. $v = 0$, in the entire domain. This implies that the presence of the opposite coastline is not essential: the Kelvin wave in Eq. (4.17a) also exists as a wave solution in a semi-infinite water domain bounded by a single straight coastline at $y = 0$.
- Shore-parallel co-range lines, along which $\tilde{\eta}(y)$ is constant, and shore-normal co-phase lines, along which $\exp(ikx)$ is constant (bottom panel of Fig. 4.5a).
- Dynamics of a progressive shallow water wave in the along-coast direction and *geostrophy* in the shore-normal direction. The latter implies a balance between the cross-shore pressure-gradient acceleration $-g\frac{\partial \eta}{\partial y}$ and the Coriolis acceleration fu of the alongshore flow (see Eq. (4.4b) and recall that $v = 0$).

Bottom friction ($r > 0$, so $\gamma \neq 1$) distorts the above picture (Fig. 4.5b). The along-channel velocity has a phase lead with respect to the surface elevation. The wave number $k = k_r + ik_i$ is complex, implying exponential amplitude decay in the direc-

tion of propagation as well as a reduced wave speed

$$c = \frac{\sigma}{k_\mathrm{r}} = \pm\sqrt{gh}\left[\frac{1}{2} + \frac{1}{2}\sqrt{1 + \left(\frac{r}{\sigma h}\right)^2}\right]^{-1/2}, \qquad (4.19)$$

and, hence, a shorter wavelength $\lambda = 2\pi/k_\mathrm{r}$. The dependency of wave speed on tidal frequency demonstrates that bottom friction makes the wave dispersive. Also cross-channel decay is affected, but the absence of cross-channel flow ($v = 0$) continues to hold in the entire domain. The above is reflected in the co-range and co-phase lines, which become skewed and no longer perpendicular (bottom panel of Fig. 4.5a).

To illustrate these Kelvin wave properties in a more quantitative sense, let us turn to the UK East Coast. The shore-parallel co-range lines and shore-normal co-phase lines in Fig. 4.2 suggest a near-perfect Kelvin wave propagating southward. Here we shall combine coastal data from the UK Admiralty Tide Tables (Admiralty 2009) with Kelvin wave theory to estimate tidal wavelength, water depth, Rossby deformation radius and coastal velocity amplitudes.

From the tidal phases as observed at coastal tide stations between Helmsdale and Hunstanton (Fig. 4.6) and using $k = \frac{\mathrm{d}\varphi}{\mathrm{d}x}$ with phase φ as introduced in Eq. (4.2), we thus find a wavelength estimate of $\lambda_{M2} = 1.05 \times 10^3$ km. Assuming a frictionless Kelvin wave speed of $c = \lambda/T = (gh)^{1/2}$, this corresponds to an 'effective' water depth of 57 m. In turn, with $\theta \sim 55°$N as typical latitude, we obtain a Rossby deformation radius of $R \sim 197$ km. This suggests that the tidal range is halved roughly at a distance of $R \ln 2 \approx 137$ km from the coast. As shown by Table 4.3, redoing this for the other constituents (S2, K1, O1) leads to roughly similar values of h and R.

As an alternative (not carried out here), one may also estimate the Rossby deformation radius directly from the co-range lines in Fig. 4.2 and use this to compute the 'effective' water depth. Finally, using $U = Z(g/h)^{1/2}$, the observed coastal tidal range of $H_{M2} \sim 1.66$ m corresponds to a coastal velocity amplitude of $U_{M2} \sim 0.35$ m s^{-1}. The results for the other constituents are shown in Table 4.3.

Table 4.3 Parameters used in Kelvin wave fit of UK East Coast (Fig. 4.6)

Symbol	Description	Value				Unit(s)
		M2	S2	K1	O1	
k	Wave number	0.60	0.63	0.35	0.30	$\times 10^{-5}$ rad m^{-1}
λ	Wavelength	1.05	1.00	1.80	2.12	$\times 10^3$ km
h	'Effective' water depth	57	54	44	53	m
R	Rossby deformation radius	197	193	175	191	km
H	Coastal tidal range	1.66	0.55	0.12	0.14	m
U	Coastal velocity amplitude	0.35	0.12	0.03	0.03	m s^{-1}
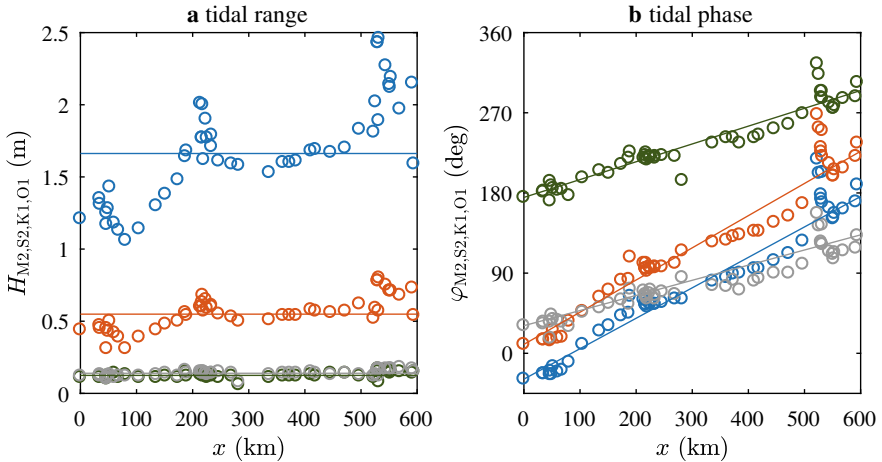
Fig. 4.6 Observations of M2 (blue circles), S2 (red), K1 (green) and O1 (grey) for coastal tide stations between Helmsdale and Hunstanton (UK, see Fig. 4.2): **a** tidal range H, **b** tidal phase φ. Data plotted as a function of the distance x on the straight line Helmsdale-Hunstanton, upon which each tide station's location has been projected ($x = 0$ corresponding to Helmsdale). The straight solid lines represent the fits of mean tidal range (left) and $\frac{d\varphi}{dx}$ (right). Data from UK Admiralty (Admiralty 2009)

4.3.3 Poincaré Waves

The third root of Eq. (4.15) corresponds to the set of infinitely many wave solutions known as *Poincaré waves*. As implied by the condition $\sin \alpha b = 0$, these modes are characterised by transverse wave numbers

$$\alpha_n = \frac{n\pi}{b}, \qquad \text{for } n = 1, 2, 3, \ldots . \tag{4.20}$$

Substitution of Eq. (4.20) into Eq. (4.12) leads to expressions for the wave number:

$$k_n^\oplus = \sqrt{\gamma^2 K^2 - \gamma^{-2} R^{-2} - \alpha_n^2}, \qquad k_n^\ominus = -k_n^\oplus, \tag{4.21}$$

which is the dispersion relationship for Poincaré waves. Here, γ, K and R are as defined in Eqs. (4.11), (4.16) and (4.18).

On the basis of Eq. (4.21), we thus identify two sets of countably infinite modes, labeled $n = 1, 2, 3, \ldots$ and characterised by wave numbers, the real and imaginary parts of which are either positive ($k_n^\oplus$) or negative ($k_n^\ominus$).

With the aid of the polarisation equations (4.9), the cross-channel structures of the surface elevation and flow field are found to be

$$\tilde{\phi}_n^\oplus = \begin{pmatrix} \tilde{\eta}_n^\oplus \\ \tilde{u}_n^\oplus \\ \tilde{v}_n^\oplus \end{pmatrix} = \begin{pmatrix} Z \\ \frac{k_n^\oplus}{\gamma K} U \\ 0 \end{pmatrix} \cos \alpha_n y + \begin{pmatrix} \frac{-f k_n^\oplus}{\alpha_n \gamma^2 \sigma} Z \\ \frac{-f K}{\alpha_n \gamma \sigma} U \\ \frac{i\gamma K}{\alpha_n} \left[1 - \frac{k_n^{\oplus 2}}{\gamma^2 K^2} \right] U \end{pmatrix} \sin \alpha_n y. \tag{4.22}$$

For the other family, replace $\oplus$ with $\ominus$. As degree of freedom, we have chosen to specify the elevation amplitude Z at $(x, y) = (0, 0)$. The velocity scale U is as defined in Eq. (4.17a).

Let us now highlight the key properties of Poincaré waves, first for the case without bottom friction ($r = 0$, so $\gamma = 1$, Figs. 4.7 and 4.8).

- Unlike frictionless Kelvin waves, Poincaré waves are dispersive. This is reflected in the curved lines of σ versus k (Figs. 4.8a, c, d).
- Governed by the sinusoidal structure for the cross-channel flow velocity amplitude, the structures of elevation are also harmonic. The phase lag of 90° between u and v implies that the end point of the depth-averaged velocity vector describes an elliptical path during a tidal cycle.
- In the absence of bottom friction, Poincaré waves are either *free* (characterised by a real wave number $k_n = k_{n,r}$) or *evanescent* (purely imaginary wave number $k_n = i k_{n,i}$). This is seen from the filled dots in Figs. 4.8a, b. For evanescent waves, the amplitude decays exponentially in the positive or negative x-direction with an e-folding decay length that is given by $L_n = |k_{n,i}|^{-1}$.
- For any channel system, there is always a finite number $n_\star$ of free modes (possibly zero, $1 \leq n \leq n_\star$) and an infinite number of evanescent modes ($n > n_\star$). For the
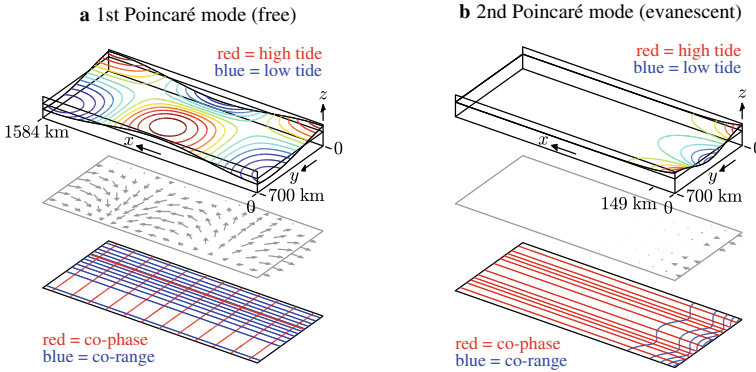
Fig. 4.7 Visualisation of Poincaré waves, in a channel section of uniform width and depth in the Northern Hemisphere (without bottom friction): **a** example of free mode propagating from right to left ($n = 1$), **b** example of evanescent mode exponentially decaying from right to left ($n = 2$). Analogous to Fig. 4.5, the sketch contains snapshots of surface elevation (top, with high tide in red and low tide in blue) and depth-averaged velocity (middle), as well as co-range and co-phase lines (blue and red in bottom panel, resp.). Parameter values as in Table 4.2, with channel width chosen such that the first mode is free and the second evanescent

example in Fig. 4.8, it follows that $n_\star = 1$. For these evanescent modes, the decay length L_n decreases with increasing n. In other words, the evanescent mode with the lowest index has the largest decay length, namely $L_{n_\star+1}$.
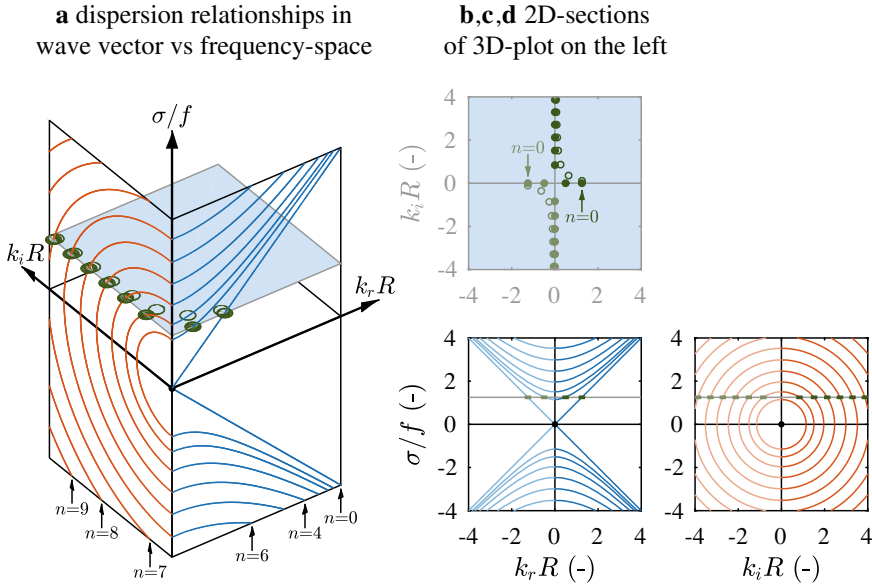
- In particular, provided that $\sigma > |f|$, there is a critical channel width b_{crit}, given by

$$b_{\text{crit}} = \pi \sqrt{\frac{gh}{\sigma^2 - f^2}}\,, \tag{4.23}$$

such that all Poincaré modes are evanescent if $b < b_{\text{crit}}$. Conversely, a finite number of free modes exist if $b > b_{\text{crit}}$. This follows from requiring the square root in Eq. (4.21) to have a vanishing argument for $n = 1$. Equivalently, one may derive a critical depth h_{crit} such that all Poincaré modes are evanescent if $h > h_{\text{crit}}$. Finally, for $\sigma \leq |f|$, all Poincaré modes are evanescent regardless width or depth.

Analogous to the Kelvin wave, the inclusion of bottom friction distorts the above picture. The wave numbers experience a shift in the complex plane: the free modes attain a nonzero imaginary part and the evanescent modes a nonzero real part (open dots in Figs. 4.8a, b). Also, changes in phase of velocity with respect to elevation take place.

a dispersion relationships in
wave vector vs frequency-space

b,c,d 2D-sections
of 3D-plot on the left

Fig. 4.8 Dispersion relationships (4.16) and (4.21) of Kelvin and Poincaré modes presented in dimensionless form. Plotted is the dimensionless frequency σ/f versus the real and imaginary parts ($k_r R$, $k_i R$) of the dimensionless wave number (with Rossby deformation radius R): **a** Three-dimensional visualisation in ($k_r R$, $k_i R$, σ/f)-space (without bottom friction). The filled dots on the light-blue plane show the modes obtained for $\sigma/f = 1.25$, with free modes along the real axis and evanescent modes along the imaginary axis. The indices at the bottom show the Kelvin mode ($n = 0$) and Poincaré modes ($n = 1, 2, 3, \ldots$). **b** Two-dimensional plot of these modes ($\sigma/f = 1.25$) in the complex ($k_r R$, $k_i R$)-plane, with $n = 0$ denoting the Kelvin modes. The open dots in a,b show how the modes shift when bottom friction is included ($\mu = \frac{r}{\sigma h} = 0.18$). **c,d** 2D-sections showing σ/f versus *real* part $k_r R$ (blue, whenever kR is real) and *imaginary* part $k_i R$ (red, whenever kR is imaginary). Parameter values in Table 4.2, corresponding to a dimensionless channel width $b/R = 5.6$

4.3.4   Wave Solutions with a Transverse Topographic Step

Wave solutions in a channel section with a single cross-channel topographic step (at $y = y_s$, see Sect. 4.2 in Fig. 4.4) consist of a solution in the lower compartment and one in the upper compartment (Roos and Schuttelaars 2009). We thus extend Eq. (4.8) to

$$
\phi = \begin{cases} \mathrm{Re}\left\{\tilde{\phi}(y)\exp(\mathrm{i}[kx - \sigma t])\right\} & \text{for } 0 \leq y \leq y_s \text{ ('lower')}, \\ \mathrm{Re}\left\{\tilde{\phi}'(y)\exp(\mathrm{i}[kx - \sigma t])\right\} & \text{for } y_s \leq y \leq b \text{ ('upper')}, \end{cases} \tag{4.24}
$$

with wave number k and cross-channel structures $\tilde{\phi}(y) = (\tilde{\eta}, \tilde{u}, \tilde{v})$ and $\tilde{\phi}'(y) = (\tilde{\eta}', \tilde{u}', \tilde{v}')$. Quantities in the upper compartment are denoted with a prime, those

in the lower compartment without a prime. Apart from different depths $h \neq h'$, we also allow different friction coefficients $r \neq r'$.

Since ϕ must be a solution to the model equations (4.4), each component must also satisfy the extended Klein-Gordon equation (4.10). Additionally, the solution must satisfy the closed boundary condition (4.5a) and the matching conditions across the topographic step in Eq. (4.7b). In fact, the latter force the wave number k in Eq. (4.24) to be identical in both compartments.

For a given wave number k (to be determined below), the cross-channel structure of the cross-channel velocity is written as

$$\tilde{v}(y) = \frac{C \sin \alpha y}{h \sin \alpha y_\mathrm{s}}, \qquad \tilde{v}'(y) = \frac{C \sin \alpha' y'}{h' \sin \alpha' y'_\mathrm{s}}, \qquad \text{with } y' = y - b, \qquad (4.25)$$

in which we have introduced the coefficients

$$\alpha = \sqrt{\gamma^2 K^2 - \gamma^{-2} R^2 - k^2}, \qquad \alpha' = \sqrt{\gamma'^2 K'^2 - \gamma'^{-2} R'^2 - k^2}. \qquad (4.26)$$

The solution in Eq. (4.25) has been constructed such that it automatically satisfies all of the above conditions, except continuity of elevation across the topographic step, i.e. except $\tilde{\eta}(y_\mathrm{s}) = \tilde{\eta}'(y_\mathrm{s})$. This last requirement serves as solvability condition for the existence of non-trivial wave solutions. A numerical search routine, minimising $|\tilde{\zeta}(y_\mathrm{s}) - \tilde{\zeta}'(y_\mathrm{s})|$, is then used to identify the wave numbers k, thus fixing the values of the coefficients α and α' according to Eq. (4.26). Expressions for the cross-channel structures of surface elevation $\tilde{\eta}$ and $\tilde{\eta}'$ as well as along-channel velocity $\tilde{u}$ and $\tilde{u}'$ are given in the Appendix.

The procedure outlined above identifies modified versions of each Kelvin and Poincaré mode in the two families, characterised by a shift in wave number and a deformed cross-channel structure. The presence of the two closed channel boundaries prevents new modes from arising here, e.g. the so-called double Kelvin wave that may propagate along a depth discontinuity in an infinite water domain (Longuet-Higgins 1968).

4.4 Amphidromic Patterns in Semi-enclosed Basins

In this section, we demonstrate how superpositions of the wave solutions derived in Sect. 4.3 explain amphidromic patterns in semi-enclosed basins. As an important first result, it is shown analytically that two Kelvin waves in a channel already produce an amphidromic system (Sect. 4.4.1). Then, Taylor's problem of Kelvin wave reflection in a semi-enclosed basin is addressed, presenting the solution method (Sect. 4.4.2) and properties of the solution (Sect. 4.4.3), the latter including application to the Gulf of California. In fact, an extended version of Taylor's problem is considered here, as we include bottom friction (Rienecker and Teubner 1980) and topographic steps (Roos and Schuttelaars 2009) (as well as a finite basin length). The Gulf of

California serves as a typical example with an important role for both bottom friction and topographic variations.

4.4.1   Superposition of Two Kelvin Waves

Consider the situation with two Kelvin waves, simultaneously travelling in opposite directions along opposite coastlines of a channel section of uniform width and depth. Following Eqs. (4.8) and (4.17), the surface elevation of this superposition is written as

$$\eta = \mathrm{Re}\big\{Z_0^{\oplus} \exp(-\delta y) \exp(\mathrm{i}[k_0^{\oplus} x - \sigma t])$$
$$+ Z_0^{\ominus} \exp(-\delta[b - y]) \exp(\mathrm{i}[k_0^{\ominus} x - \sigma t])\big\}, \qquad (4.27)$$

with coastal amplitudes $Z_0^{\oplus} = |Z_0^{\oplus}| \exp(\mathrm{i}\varphi_0^{\oplus})$ and $Z_0^{\ominus} = |Z_0^{\ominus}| \exp(\mathrm{i}\varphi_0^{\ominus})$, wave numbers $k_0^{\oplus} = -k_0^{\ominus} = k_{\mathrm{r}} + \mathrm{i}k_{\mathrm{i}}$ and complex coefficient $\delta = \delta_{\mathrm{r}} + \mathrm{i}\delta_{\mathrm{i}} = \gamma^{-1} f/(gh)^{-1/2}$. Equation (4.27) can be rewritten into real notation according to

$$\eta = Z \big[\exp(-\psi) \cos(\xi - \chi) + \exp(\psi) \cos(\xi + \chi)\big], \qquad (4.28)$$

where we have introduced the short-hand notation

$$Z = |Z_0^{\oplus}| \exp(-\delta_{\mathrm{r}} y_{\star}), \qquad \text{with } y_{\star} = \frac{1}{2}b + \frac{1}{2}\delta_{\mathrm{r}}^{-1} \log(|Z_0^{\oplus}|/|Z_0^{\ominus}|), \quad (4.29\mathrm{a})$$
$$\psi = k_{\mathrm{i}}x + \delta_{\mathrm{r}}(y - y_{\star}), \qquad\qquad\qquad\qquad\qquad\qquad (4.29\mathrm{b})$$
$$\xi = k_{\mathrm{r}}x - \delta_{\mathrm{i}}(y - \tfrac{1}{2}b) + \tfrac{1}{2}[\varphi_0^{\oplus} - \varphi_0^{\ominus}], \qquad\qquad\qquad (4.29\mathrm{c})$$
$$\chi = \sigma t + \tfrac{1}{2}\delta_{\mathrm{i}}b - \tfrac{1}{2}[\varphi_0^{\oplus} + \varphi_0^{\ominus}]. \qquad\qquad\qquad\qquad (4.29\mathrm{d})$$

Using trigonometric identities, we may now rewrite Eq. (4.28) into the form of Eqs. (4.1)–(4.2), i.e.

$$\eta(x, y, t) = H(x, y) \cos(\sigma t - \varphi(x, y)), \qquad (4.30)$$

with analytical expressions for tidal range H and phase φ:

$$H(x, y) = 4Z \big(\cosh^2 \psi \cos^2 \xi + \sinh^2 \psi \sin^2 \xi\big), \qquad (4.31\mathrm{a})$$
$$\tan \varphi(x, y) = \tanh \psi \tan \xi. \qquad\qquad\qquad\qquad (4.31\mathrm{b})$$

This result reveals the existence of amphidromic points, characterised by zero tidal range (Fig. 4.9). The requirement $H = 0$ implies (i) $\psi = 0$ and (ii) $\xi = (p + \frac{1}{2})\pi$ with integer p. The former condition defines a line through $(x, y) = (0, y_{\star})$ that is either coast-parallel (in the case without bottom friction; Fig. 4.9a) or tilted (with bottom friction; Fig. 4.9b). The latter condition locates the actual amphidromes on
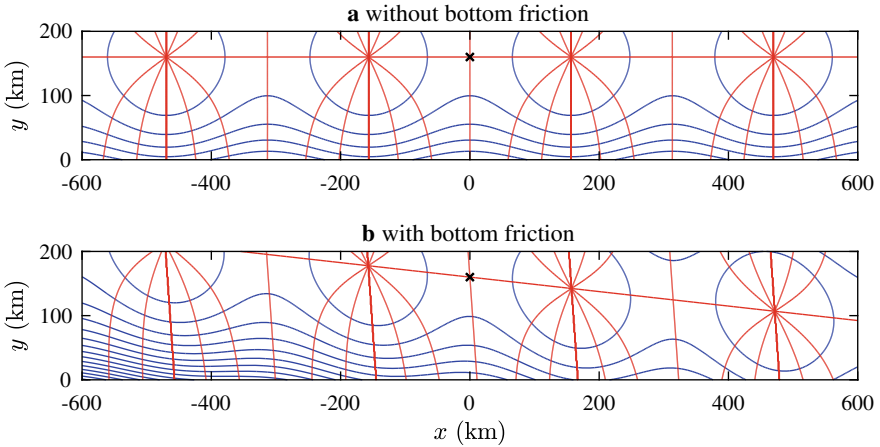
Fig. 4.9 Amphidromic chart (red=co-phase, blue=co-range) of the superposition of two Kelvin waves in a channel section of uniform width and depth according to the analytical solution in Eq. (4.31). **a** Without bottom friction, the amphidromic points are found on a coast-parallel line, here located slightly off the centerline (due to different coastal amplitudes). **b** With bottom friction, the amphidromes are located on a tilted line, leading to real and virtual amphidromes. In both examples, the point $(x, y) = (0, y_\star)$ in Eq. (4.29a), where both amplitudes are equal, is denoted with a black cross (here, $y_\star = 160$ km). Parameter values as in Table 4.2

this line, which may be inside or outside the channel (real or virtual). The presence of a transverse topographic step (as in Sect. 4.2 in Fig. 4.4) would distort the above amphidromic pattern, since the two Kelvin waves will then have slightly different wavelengths.

We conclude that the interference pattern of two Kelvin waves, propagating in opposite directions, produces an amphidromic system. The cross-channel positions of the amphidromic points depend on the relative amplitudes, which in turn is also affected by bottom friction. However, the case of a basin with a closed end (Fig. 4.4a, b) is not solved by any superposition of two Kelvin waves, as they cannot satisfy the closed boundary condition in Eq. (4.5b). How to overcome this difficulty, often referred to as *Taylor's problem*, is tackled in the next subsection.

4.4.2 Solution to Extended Taylor Problem

Let us now turn to the so-called *Taylor problem* (Taylor 1922) of tidal motion in a semi-enclosed basin of uniform width, with a closed boundary at $x = 0$. The classical version of this problem concerns an infinitely long basin of uniform depth, forced by an incoming Kelvin wave from $+\infty$, in the absence of bottom friction. Here we consider a different version of the problem: as before, we include bottom friction, allow for topographic steps, and further we consider a basin of finite length ℓ with

specified elevation amplitude and phase according to Eq. (4.2) as the open boundary condition at $x = \ell$ (Fig. 4.4). In our description below, we shall first ignore the topographic steps; how to include those is explained further below.

Different from the form of the individual wave solutions of Eq. (4.8) in Sect. 4.3, the solution $\phi = (\eta, u, v)$ is now more generally written as

$$\phi = \mathrm{Re}\left\{\hat{\phi}(x, y)\exp(-\mathrm{i}\sigma t)\right\}, \tag{4.32}$$

with complex amplitudes $\hat{\phi}(x, y) = (\hat{\eta}(x, y), \hat{u}(x, y), \hat{v}(x, y))$ that depend on both horizontal coordinates x and y.

The solution is then written as a (truncated) superposition of Kelvin and Poincaré modes according to

$$\hat{\phi}(x, y) = \sum_{n=0}^{N} a_n^{\oplus}\tilde{\phi}_n^{\oplus}(y)\exp(\mathrm{i}k_n^{\oplus}x) + \sum_{n=0}^{N} a_n^{\ominus}\tilde{\phi}_n^{\ominus}(y)\exp(\mathrm{i}k_n^{\ominus}[x - \ell]), \tag{4.33}$$

with nonzero[5] truncation number N and involving $2(N + 1)$ dimensionless complex coefficients $a_n^{\oplus}$ and $a_n^{\ominus}$. By construction, the solution presented here automatically satisfies the model equations (4.4) and the closed boundary conditions at $y = 0, b$ in Eq. (4.5a).

To satisfy also the two remaining conditions, i.e. the closed boundary condition at $x = 0$ in Eq. (4.5b) and the prescribed elevation amplitude and phase at $x = \ell$ in Eq. (4.6), we apply a so-called *collocation method* (Brown 1973). To this end, we define $N + 1$ lateral points $y_n = bn/N$ and we require that

$$\hat{u}(0, y_n) = 0, \qquad \hat{\zeta}(\ell, y_n) = \tfrac{1}{2}H(y_n)\mathrm{Re}\left\{\exp(\mathrm{i}\varphi(y_n))\right\} \quad \text{for } n = 0, 1, \ldots, N, \tag{4.34}$$

with tidal range H and phase φ taken from Eq. (4.6). This set of $2(N + 1)$ conditions leads to a linear system for the $2(N + 1)$ coefficients $a_n^{\oplus}$ and $a_n^{\ominus}$, which can be solved using standard techniques. It should be noted that the final solution in Eqs. (4.32) and (4.33) is independent of the value chosen for the elevation scale Z of the individual wave solutions in Eqs. (4.17) and (4.22).

Finally, some remarks on the solution method are in order.

- Generally, taking a truncation number of $N = \mathcal{O}(10)$ already produces a qualitatively correct picture of the solution (see Sect. 4.4.3). Further increasing N improves the accuracy of the solution mainly in the vicinity of the collocation points. While orthogonality conditions for Kelvin and Poincaré waves have been derived (Ripa and Zavala-Garay 1999), whether they actually form a complete set remains an open mathematical problem.

---

[5] Choosing $N = 0$ would effectively bring us back to the superposition of two Kelvin waves only, as already analysed in Sect. 4.4.1.

- The above procedure can be easily adjusted to cover the classical version of Taylor's problem. Instead of the second condition in Eq. (4.34), one should then choose a nonzero value of $a_0^\ominus$, force $a_n^\ominus = 0$ for all $n = 1, 2, \ldots, N$ and solve the set of $N + 1$ remaining equations resulting from the first condition in Eq. (4.34).
- Alternatively, the presence of an along-basin topographic step, at some $x = x_s$, is incorporated by defining separate expressions as in Eq. (4.33) for each compartment (Roos and Schuttelaars 2009). The increase in number of coefficients is then exactly balanced by the additional matching conditions across the step: one should require Eq. (4.7a) to be satisfied at all points (x_s, y_n) for $n = 0, 1, \ldots, N$.
- The presence of a cross-basin topographic step, at some $y = y_s$ poses no complications either. One can readily take the modified wave solutions as derived in Sect. 4.3.4. One should choose the truncation number N such that the transverse position y_s of the step does not coincide with any of the collocation points, since the longitudinal velocity is not uniquely defined there.

4.4.3 Application to Basins Around the World

A three-dimensional sketch of the solution to the Taylor problem is shown in Fig. 4.10. It shows a snapshot of the surface elevation (top) and the corresponding instantaneous flow field (bottom). For simplicity, this pertains to the classical Taylor problem, i.e. excluding bottom friction and imposing an incoming Kelvin wave rather than a prescribed elevation profile at the open boundary.

As it turns out, near the basin's closed end the depth-averaged flow velocity vector describes ellipses (also shown in the bottom panel of Fig. 4.10). Physically, this is due to the Coriolis effect: it effectively turns the reflection of the tidal wave at the basin's head into a cyclonic rotation of a Kelvin wave. Mathematically, this is seen in the Poincaré modes generated to satisfy the closed boundary condition at the basin's head ($x = 0$). In this subcritical case ($b < b_{crit}$) all Poincaré modes are evanescent, implying that further away the solution is effectively the superposition of the incoming and reflected Kelvin waves, for which the flow aligns with the along-basin direction. This alignment is actually visible because the decay length of the first Poincaré mode is smaller than the basin length.

Next, the four examples in Fig. 4.11 show the solution to the extended Taylor problem, restricting to the amphidromic charts. They particularly illustrate the (separate and combined) effects of including bottom friction and a shallow region near the basin's head. For this example with a subcritical basin width ($b < b_{crit}$, so all Poincaré modes are evanescent[6]), we highlight the following properties.

---

[6] As pointed in Sect. 4.3.3, this definition applies to the frictionless case.
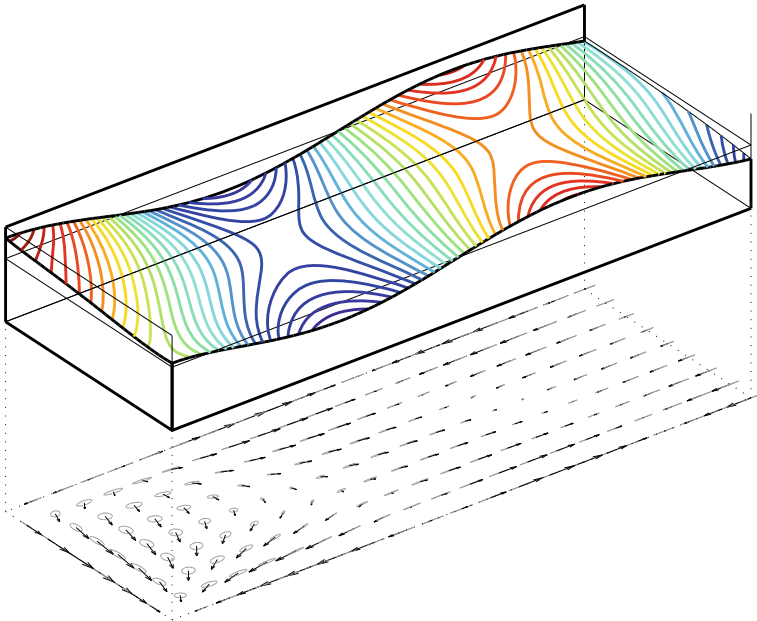
Fig. 4.10 Example of Taylor's solution, showing snapshot of the surface elevation (top, high tide in red, low tide in blue), as well as the corresponding depth-averaged flow vector (bottom), which describes ellipses during the tidal cycle. The basin's closed end is on the left-hand side, the open boundary on the right-hand side

- Without bottom friction, the reflected Kelvin wave has the same amplitude as the incoming Kelvin wave. As a result, amphidromic points are on the centerline of the basin.[7]
- Bottom friction distorts the picture in a similar fashion as in the plain superposition of two Kelvin waves (see Sect. 4.4.1 and Fig. 4.9). However, now the two Kelvin waves are connected by the reflection process at the closed end, which involves evanescent Poincaré modes bound to $x = 0$. As a result, amphidromic points shift toward the lower coastline ($y = 0$).
- Including a shallow region near the basin's head may lead to tidal amplification, and thus to higher values of the tidal range.
- The combined effect of bottom friction and the shallow part may enhance the shift of amphidromes away from the centerline (also see application to the Gulf of California below).

---

[7] For supercritical basins, i.e. basins with $b > b_{crit}$, this is not true since tidal wave energy is also reflected in a free Poincaré mode. This leads to a more complex amphidromic pattern resulting from the interference of these modes.
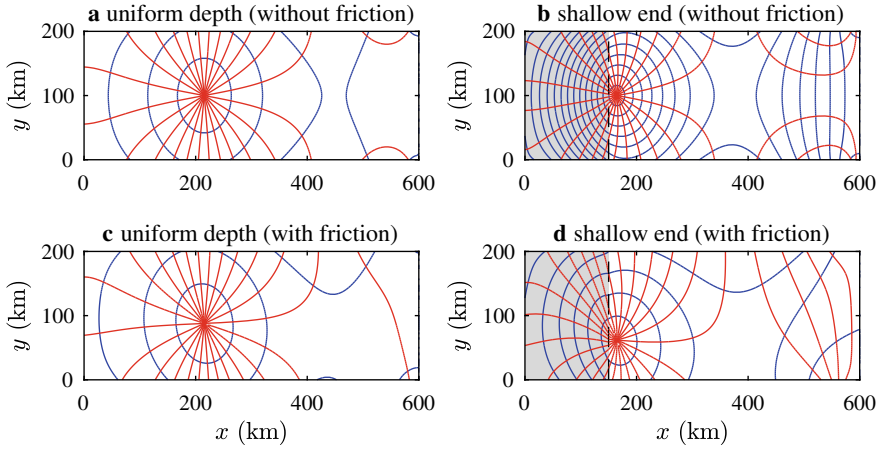
Fig. 4.11 Four examples of amphidromic charts (red=co-phase, blue=co-range) showing the solution to the extended Taylor problem. **a** Reference case with uniform depth of 40 m, no bottom friction. **b** Including a shallow zone near the basin's head (20 m deep, grey shade), no friction. **c** Uniform depth, now including friction. **d** Including both shallow zone and friction. Parameter values as in Table 4.2. All solutions are forced by an M2-tide with a uniform tidal range of $H = 1$ m at the open boundary (on the right). Contours are shown every 0.5 m

To apply and test our model, let us consider the Gulf of California (Hendershott and Speranza 1971; Carbajal and Backhaus 1998; Marinone 2000). This elongated basin is characterised by mixed semi-diurnal tides and a large tidal range in the northern part (spring tidal range close to 10 m). Typical is the virtual amphidromic point occurring for the semi-diurnal tides (Fig. 4.3).

Our procedure consists of the following four steps (Roos and Schuttelaars 2009).

1. We define a rectangular model geometry $PQRS$ that provides a good fit of the coastline. It has length $\ell = 1223$ km, width $b = 166$ km and an orientation/positioning as shown in Fig. 4.12a.
2. We perform orthogonal projections of the available tide stations on the model boundary (Fig. 4.12a). This enables us to plot observed ranges and phases (Carbajal and Backhaus 1998) as a function of a single coordinate: the distance along the perimeter $PQRS$.
3. Based on bathymetry (Fig. 4.12), we choose a division in two compartments, separated by a single longitudinal topographic step at $x_s = 350$ km: a shallow compartment with $h_1 = 100$ m near the basin's head and a deep compartment with $h_2 = 1200$ m.
4. Using a representative latitude $\theta = 27.5°$N, we perform model simulations varying both amplitude and phase of the incoming Kelvin wave. Note that this implies a different open boundary condition than in Eq. (4.2).

Results for the M2, S2, K1 and O1-tides are shown in Figs. 4.12c-f. In particular, the non-monotonous curve of the semi-diurnal phases φ_{M2} and φ_{S2} along the basin perimeter indicates the presence of a *virtual amphidromic point* (see Sect. 4.1 and Fig. 4.3). Such a pattern occurs when the amplitude of the reflected Kelvin wave is much weaker than that of the incoming Kelvin wave. Physically, this is caused by the enhanced dissipation due to bottom friction of the (locally amplified) tide in the shallow zone near the basin's head. This mechanism is also illustrated by the example in Fig. 4.10, although in that example the dissipation is too weak for the amphidrome to become virtual.

We conclude that our extended Taylor model, in spite of its strong schematisations, can adequately reproduce the patterns of tidal range and phase, as observed along the Gulf of California's coastline.

In other examples, the amphidromic patterns in basins with other length, widths, water depth and tidal ranges can be notably different. For example, the Adriatic Sea also has a shallow zone near the head, but tides and hence tidal dissipation are relatively weak, such that the amphidromes are still real and not virtual (Hendershott and Speranza 1971; Roos and Schuttelaars 2009). Alternatively, the asymmetric depth profile in the Persian Gulf leads to different Kelvin wavelengths on either side of the basin of the incoming and reflected Kelvin waves. Finally, basins characterised by (stepwise) variations in basin width are touched upon in Sect. 4.5.

4.5 Discussion

The model approach described in this chapter has been introduced as *idealised process-based* (Sect. 4.1), in other texts also referred to as exploratory (Murray 2003). This choice is motivated by our goal to provide a generic explanation of the amphidromic patterns starting from the physical processes. Here, the obtained insights immediately stem from the structure of the solution, i.e. a superposition of fundamental wave solutions. These wave solutions can be found analytically, which greatly facilitates interpretation and understanding of the tidal dynamics. As a specific example, we highlight the identification of the Rossby deformation radius $R = \sqrt{gh}/|f|$ as typical length scale for cross-shore decay of a Kelvin wave.

One of the challenges in idealised process-based modelling is thus to seek schematisations of model geometry and process formulations that allow for efficient and insightful solution techniques, while still realistic for the problem at hand. Examples in our extended Taylor model are the linearised bottom stress parameterisation, as well as the use of rectilinear coastlines and stepwise topographic changes. Clearly, too strong schematisation jeopardise model validity. For example, other studies allowed stepwise width variations have been adopted, e.g., to model the Labrador Sea/Davis Strait/Baffin Bay system (Godin 1965) and the North Sea (Roos et al. 2011).
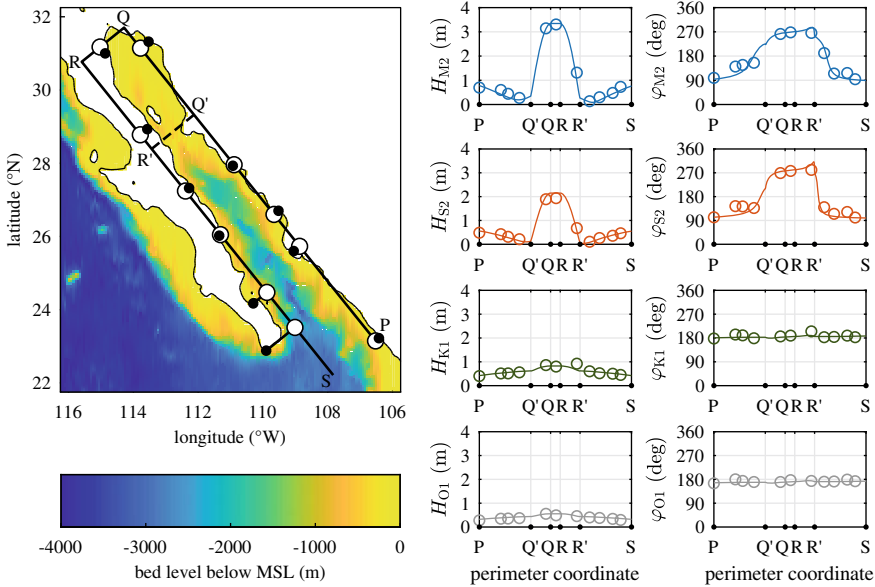
Fig. 4.12 Left: bathymetric chart of the Gulf of California with shallow region near closed end. Also shown is the rectangular model basin $PQRS$ with topographic step $Q'R'$ (dashed line) as well as tide stations (black dots) and their projections onto the model basin boundary (open circles). Right: comparison between model results (solid line) and observations (Carbajal and Backhaus 1998) (open circles). From top to bottom, this is done for the range and phase of M2, S2, K1 and O1, plotted as a function of the perimeter coordinate along $PQRS$

This idealised modelling approach contrasts with complex simulation models, which adopt state-of-the-art process formulation in numerical techniques aimed at accurate solutions with a high level of detail. We argue that, ideally, the two approaches are used in support of each other: complex models to reveal patterns, idealised models to unravel the underlying physics of the patterns found.

The knowledge and insights on barotropic tides as presented in this chapter constitute a basis for further studies that involve tides. For example, models have been developed to investigate the dynamics of secondary, nonlinear tides that are generated by nonlinear terms in the equations of motion (Iannello 1977; Parker 1993; Maas and Doelman 2002). Nonlinear tides include overtides, which are higher harmonics of a principal tidal constituent (e.g., M4, M6 are overtides of M2) and tidal residuals. Their manifestation implies that tidal records are asymmetrical, e.g. they show different durations of flood and ebb periods and/or different peak flood currents and ebb currents. Tides also nonlinearly interact with wind-driven flow (tide-surge interactions), wind waves and river flow (tide-fluvial interactions). These aspects are reviewed by Talke and Jay (2020).

Asymmetry of tidal currents is an important driver of net transport of matter, such as salt, nutrients and pollutants. An interesting application in this regard concerns the

demonstration of chaotic spreading of passive particles in a confined channel due to a simple current field that consists of a spatially uniform M2 tide and an alternating series of tidal residual eddies (Ridderinkhof and Zimmerman 1992). Furthermore, in shallow seas tidal currents are often sufficiently strong to erode sediment from the bottom and, when the currents are asymmetrical, they will also cause net transport of that sediment. These processes lead to the formation of turbidity maxima in estuaries (Burchard et al. 2018), and the emergence of bottom patterns: tidal sand ridges (De Swart and Yuan 2019), sand waves (Besio et al. 2008), tidal flats and bars (Seminara 2010), ebb-tidal deltas (De Swart and Zimmerman 2009), etcetera.

The theory of tides is further abundantly used to understand, reconstruct and predict alterations of tidal characteristics in seas and oceans. Nowadays, such alterations typically result from a mixture of naturally and anthropogenically induced changes in environmental conditions that occur on a wide spectrum of time scales. Examples are fluctuations in wind and river discharge, geometrical changes due to changes in mean sea level and shifts in positions of coastlines, as well as geometrical changes caused by construction of dams and dikes, deepening of fairways. Specific examples of studies that deal with changes in tides are given in the review by Talke and Jay (2020).

Tides are also an important source of turbulence, both directly and indirectly. The direct way is that turbulence is produced by the stress that tidal currents exert on a rough bottom. A more indirect way is through internal tides, which are generated by barotropic tides in stratified waters (density varies with depth) with an irregular bottom topography (Gerkema 2019). These internal waves break at steep slopes, such as those of underwater sea mountains and continental slopes, thereby creating turbulence. These turbulent motions are essential for the maintenance of the large-scale thermohaline circulation in the ocean and thus for the Earth's climate (Munk and Wunsch 1998).

4.6 Conclusions

Tides constitute a fascinating phenomenon of both theoretical and practical interest. Using idealised process-based models, solving only the essential physics on strongly schematised geometries, we have produced the gross features of tidal patterns in coastal basins around the world. The structure of the presented solutions, i.e. a superposition of fundamental wave solutions (Kelvin and Poincaré modes), leads to the following insights.

- The *Coriolis effect* is responsible for the typical cross-shore decay of tidal range away from the coast, a typical Kelvin wave property, and thus for the cyclonic wave propagation around amphidromic points in (sufficiently wide) semi-enclosed basins. Near the basin's closed end, tidal currents are elliptical, which is associated with the excitation of Poincaré waves.

- Dissipation due to *bottom friction* mainly causes a decay of tidal range in the direction of tidal wave propagation, implying a shift in the amphidromic points.
- *Topographic effects*, e.g. due to abrupt changes in depth, control tidal wave speed, which may lead to tidal amplification in shallow regions. In turn, this may enhance dissipation due to bottom friction, thus further affecting the amphidromic pattern.

Despite the strong schematisations, the idealised modelling approach is capable of grossly reproducing tidal patterns as observed in, e.g., the Gulf of California. Tidal patterns act as drivers in other studies of, e.g., morphodynamics, mixing and spreading of particles. Finally, the obtained insights and modelling techniques can be used to better understand the influence of large-scale changes due to climate change and large-scale human intervention.

Appendix

Wave Solutions in Channel with Topographic Step

The cross-channel structures of elevation and along-channel velocity of the wave solutions in an infinite channel with a single transverse topographic step (Sect. 4.3.4) are given by

$$\tilde{\eta}(y) = \frac{iC[f^2 - \gamma^4\sigma^2]\left[\alpha\gamma^2\sigma\cos\alpha y - fk\sin\alpha y\right]}{gh[\alpha^2\gamma^4\sigma^2 + f^2k^2]\sin\alpha y_s}, \tag{4.35a}$$

$$\tilde{u}(y) = \frac{iC[f^2 - \gamma^4\sigma^2]\left[\alpha k\cos\alpha y - \frac{f\sigma}{gh}\sin\alpha y\right]}{h[\alpha^2\gamma^4\sigma^2 + f^2k^2]\sin\alpha y_s}. \tag{4.35b}$$

These expressions follow from subsequently combining the cross-channel velocity solution in Eq. (4.25) with the second polarisation equation (4.9b), and then substituting the result (4.35a) in the the first polarisation equation (4.9a). Expressions for $\tilde{\eta}'(y)$ and $\tilde{u}'(y)$ valid in the upper compartment are readily obtained by replacing the quantities $(\alpha, \gamma, h, y, y_s)$ in the above with $(\alpha', \gamma', h', y', y'_s)$.

References

Admiralty, British. 2009. *NP201-2010 Admiralty Tide Tables 2010, Volume 1*. United Kingdom Hydrographic Office.

Besio, G., P. Blondeaux, M. Brocchini, S.J.M.H. Hulscher, D. Idier, M.A.F. Knaapen, A.A. Németh, P.C. Roos, and G. Vittori. 2008. The morphodynamics of tidal sand waves: a model overview. *Coastal Engineering* 55 (7–8): 657–670.

Brown, P.J. 1973. Kelvin-wave reflection in a semi-infinite canal. *Journal of Marine Research* 31 (1): 1–10.

Burchard, H., H.M. Schuttelaars, and D. Ralston. 2018. Sediment trapping in estuaries. *Annual Review of Marine Science* 10: 371–395.

Carbajal, N., and J.O. Backhaus. 1998. Simulation of tides, residual flow and energy budget in the Gulf of California. *Oceanologica Acta* 21 (3): 429–446.

Davies, A.M. and S.C.M. Kwong. 2000. Tidal energy fluxes and dissipation on the European continental shelf. *Journal of Geophysical Research: Oceans* 105(C9): 21,969–21,989.

De Swart, H.E., and B. Yuan. 2019. Dynamics of offshore tidal sand ridges, a review. *Environmental Fluid Mechanics* 19 (5): 1047–1071.

De Swart, H.E., and J.T.F. Zimmerman. 2009. Morphodynamics of tidal inlet systems. *Annual Review of Fluid Mechanics* 41(7): 203–229.

Friedrichs, C.T. 2020. Barotropic tides in channelized estuaries. In *Contemporary issues in estuarine physics*, ed. A. Valle-Levinson, 27–61. Cambridge: Cambridge University Press.

Gerkema, T. 2019. *An introduction to tides*. Cambridge: Cambridge University Press.

Godin, G. 1965. The M2 tide in the Labrador Sea, Davis Strait and Baffin Bay. *Deep Sea Research* 12(4): 469–477.

Hendershott, M.C., and A. Speranza. 1971. Co-oscillating tides in long, narrow bays; the Taylor problem revisited. *Deep Sea Research* 18(10): 959–980.

Iannello, J.P. 1977. Tidally induced residual currents in estuaries of constant breadth and depth. *Journal of Marine Research* 35: 755–786.

Longuet-Higgins, M.S. 1968. On the trapping of waves along a discontinuity of depth in a rotating ocean. *Journal of Fluid Mechanics* 31(3): 417–434.

Maas, L.R.M., and A. Doelman. 2002. Chaotic tides. *Journal of Physical Oceanography* 32(3): 870–890.

Marinone, S.G. 2000. Tidal currents in the Gulf of California: intercomparisons among two- and three-dimensional models with observations. *Ciencas Marinas* 26(2): 275–301.

Munk, W., and C. Wunsch. 1998. Abyssal recipes II: energetics of tidal and wind mixing. *Deep Sea Research* 45(12): 1977–2010.

Murray, A.B. 2003. Contrasting the goals, strategies, and predictions associated with simplified numerical models and detailed simulations. In *Prediction in geomorphology*, vol. 135, ed. R.M. Iverson and P.R. Wilcock. Geophysical Monograph, 151–165. AGU: Washington, D.C.

Parker, B.B. 1993. *Tidal hydrodynamics*. New York: Wiley.

Pedlosky, J. 1987. *Geophysical fluid dynamics*. New York: Springer.

Platzman, G.W. 1982. Ocean tides and related waves. In: *Mathematical methods in the geophysical sciences, part 2: inverse problems, dynamo theory and tides*, ed. W.H. Reid, 239–292.

Polli, S. 1960. La propagazione delle maree nell' Adriatico. Technical Report **370**, Inst. Talassogr. Estratto da: Atti del 9. Convegno dell'Associazione geofisica italiana, Roma 20–21 novembre 1959.

Prandle, D. 1982. The vertical structure of tidal currents and other oscillatory flows. *Continental Shelf Research* 1(2): 191–207.

Reynaud, J.-Y. and R.W. Dalrymple. 2012. Shallow-marine tidal deposits. In *Principles of tidal sedimentology*, eds. R.A. Davis Jr. and R.W. Dalrymple, 335–369. Dordrecht: Springer.

Ridderinkhof, W., and J.T.F. Zimmerman. 1992. Chaotic stirring in a tidal system. *Science* 258(5085): 1107–1111.

Rienecker, M.M., and M.D. Teubner. 1980. A note on frictional effects in Taylor's problem. *Journal of Marine Research* 38(2): 183–191.

Ripa, P., and J. Zavala-Garay. 1999. Ocean channel modes. *Journal of Geophysical Research: Oceans* 104(C7): 15,479–15,494.

Roos, P.C., and H.M. Schuttelaars. 2009. Horizontally viscous effects in a tidal basin: extending Taylor's problem. *Journal of Fluid Mechanics* 640: 423–441.

Roos, P.C., J.J. Velema, S.J.M.H. Hulscher, and A. Stolk. 2011. An idealized model of tidal dynamics in the North Sea: resonance properties and response to large-scale changes. *Ocean Dynamics* 61 (12): 2019–2035.

Salas-de León, D.A., N. Carbajal-Pérez, M.A. Monreal-Gómez, and G. Barrientos-MacGregor. 2003. Residual circulation and tidal stress in the Gulf of California. *Journal of Geophysical Research: Oceans* 108 (C10): 3317.

Seminara, G. 2010. Fluvial sedimentary patterns. *Annual Review of Fluid Mechanics* 42: 43–66.

Sinha, B., and R.D. Pingree. 1997. The principal lunar semidiurnal tide and its harmonics: baseline solutions for M2 and M4 constituents in the North-West European continental shelf. *Continental Shelf Research* 17 (11): 1321–1365.

Talke, S.A., and D.A. Jay. 2020. Changing tides: the role of natural and anthropogenic factors. *Annual Review of Marine Science* 12: 121–151.

Taylor, G.I. 1922. Tidal oscillations in gulfs and rectangular basins. *Proceedings of the London Mathematical Society* 20(1): 148–181.

Zongwan, X., N., Carbajal and J. Südermann,. 1995. Tidal current amphidromic system in semi-enclosed basins. *Continental Shelf Research* 15(2–3): 219–240.